Scour monitoring via turbulent open channel flow

Meas. Sci. Technol. **24** (2013) 085602 (14pp) doi:10.1088/0957-0233/24/8/085602

Scour monitoring via turbulent open channel flow

M Fisher, A Khan[1] and S Atamturktur

Glenn Department of Civil Engineering, Clemson University, Clemson, SC, USA

E-mail: abdkhan@clemson.edu

Received 15 March 2013, in final form 16 May 2013
Published 2 July 2013
Online at stacks.iop.org/MST/24/085602

Abstract
Scour is the leading cause of bridge failure in the United States. It can result in the loss of lives and costs millions to repair the damage. A novel method is proposed for monitoring scour that exploits the turbulence in natural channels. The method utilizes the dynamic pressure associated with the turbulent velocity fluctuations in the flow to excite a flexible plate. A semi-empirical model is developed to describe the interaction of turbulent open channel flow with the plate. The model describes the variation of turbulent velocity fluctuations across the flow depth in an open channel resulting in a method for determining the average dynamic pressure on the flexible plate. The dynamic response of the plate is then modeled by superimposing the response of multiple modes of the disk to the random, turbulent dynamic pressure spectrum. The model is verified considering the pressure integration across the plate surface to ensure converged solutions. Due to the uncertainties in the material properties of the plate, the experimentally determined natural frequencies and vibration measurements are used to calibrate the model. The calibrated model predictions are then compared against an independent dataset for validation. In addition to describing the physical operation of the device, the semi-empirical model is also employed to optimize the field device. Measurements made using the field device also confirmed the model results, even in a non-design, misaligned flow condition.

Keywords: fluid–structure interaction, turbulence, structural health monitoring, flow induced vibration, model development

1. Introduction

One of the most significant financial investments in any transportation infrastructure system is for the bridges that connect otherwise geographically isolated communities. Failure of these structures can have significant impacts, both in financial and human terms. The leading cause of bridge failures in the United States is due to the removal of bed material surrounding the foundations of bridge piers and abutments, a process known as scour. Scour failures, accounting for 60% of all bridge failures [1], have resulted in the direct loss of lives [2], and have accounted for hundreds of millions of dollars in repair damage [3]. Additionally, bridge failures due to scour can have a dramatic impact on the local community, with the financial impact estimated to be five times the actual repair cost [4]. Therefore, it is necessary to protect these critical infrastructure elements against scour damage.

Scour damage can be prevented by armoring the bed to reduce the amount of scour or by adjusting the river hydraulics to reduce the peak flow, requiring significant amounts of time and financial resources for implementation. Scour monitoring, however, can be implemented faster and at reduced cost relative to the other preventative measures. For this reason the Federal Highway Administration's *Highway Engineering Circular #23* lists scour monitoring as a viable countermeasure for scour critical bridges [2]. Scour at bridges occurs over time, with peak flow events progressively adding to the scour around the pier or abutment. Thus, by monitoring the history of scour at a bridge, it is possible to determine if the scour depth is approaching the critical value determined during the bridge design. As the scour depth approaches this threshold value, it is possible to begin planning the more extensive

[1] Author to whom any correspondence should be addressed.

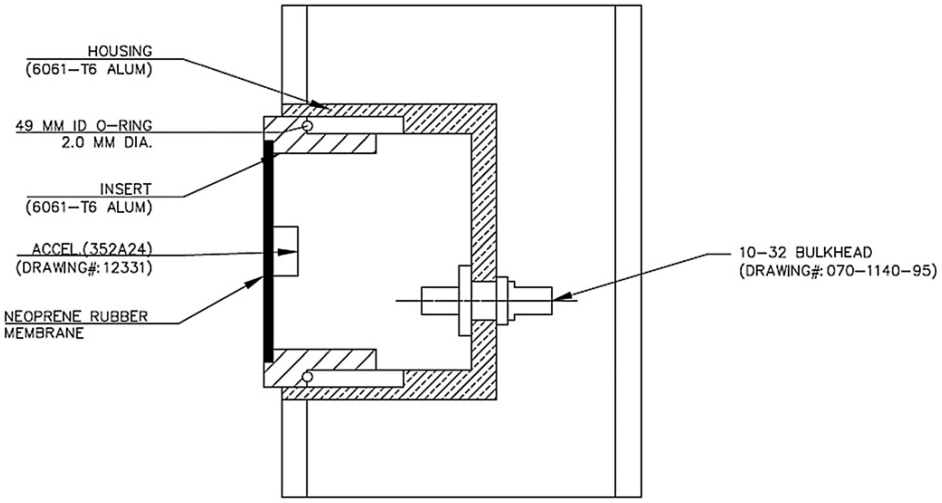

Figure 1. Schematic of field VTP configuration.

armoring or river training mechanisms required to protect the bridge.

Given the importance of scour monitoring in determining the health of the bridge related to this threshold, a novel method has been proposed and evaluated which exploits the turbulent flow inherent in natural channels [5]. The turbulent flow excites a flexible plate that is monitored with an accelerometer sensitive to low frequency vibrations. Accordingly, these sensors are called vibration-based turbulent pressure sensors (VTPs). The data collection system records the mean squared acceleration signal in the time domain for each VTP. This measured quantity is referred throughout this work as the energy content of the VTP. It has been shown that the energy content for a VTP located in the flow is one to two orders of magnitude greater than for a VTP located in the sediment [5]. In the field, the bridge is instrumented with multiple VTPs located across the depth of the piers or abutments. Thus, by monitoring the energy content profile across the channel depth, it is possible to determine whether a VTP is in the flow or if it is located in the bed. As a scour hole develops, the energy content of the VTPs uncovered by the degradation of the riverbed increases [5]. It is then possible to track the movement of the bed over time using the VTP. Additionally, the VTP has been shown to be insensitive to many of the channel conditions that can affect other common scour monitoring devices, such as temperature, salinity and suspended sediment concentrations [6].

The objective of this work is to consider in detail the physical principles behind the operation of the VTP and to describe a semi-empirical model that accounts for the interaction of the turbulent open channel flow with a flexible plate. A semi-empirical method is useful for describing the interaction of fluids and structures across a broad frequency spectrum as more complicated computational methods are limited in their application to design and optimization problems. To capture the full turbulent flow spectrum, a 3D fluid model must be capable of calculating the instantaneous velocity field. This is required to determine the dynamic response of a structure to both large and small scale turbulent eddies (low and high frequency incident forces). Only large eddy simulation (LES) or direct numerical simulation (DNS) methods are available to fully capture the velocity field [7]. These models, however, require significant computational time and resources, even without considering the structural analysis components.

The performance of a new prototype for the field is discussed in section 2. The semi-empirical model is described in detail in section 3, which is followed by a review of the verification, calibration and validation activities conducted on the model in section 4. Section 5 follows with a discussion on the use of the semi-empirical model for optimization. Pertinent conclusions from this work and avenues for further research are discussed in section 6.

2. Field prototype

A field prototype device is constructed with eight VTPs distributed along a 1 m length of the support pipe. The VTPs are spaced 10.2 cm apart and housed within removable units which are designed to aid maintenance in the field and to ensure that damage to one device does not allow water to penetrate into the undamaged VTPs. A schematic of the device is shown in figure 1. The fully assembled prototype is shown in figure 2. The accelerometers installed in the field prototype are PCB model 352A24, with a sensitivity of 10 mV/m s^{-2}. The accelerometers are connected to the bulkhead shown in figure 1, in order to provide a water tight seal through which the accelerometer signal is routed. On the interior of the support pipe, the signal is carried by a wiring harness to the top flange of the pipe, where it passes through a water tight bulkhead and into a wet-mateable fitting for connection to the data lines and the data collection units.

The fully assembled field prototype is tested in the Clemson Hydraulics Laboratory (CHL) flume to ensure the performance of the device. The tests are conducted in the channel flow with velocities ranging from 14 to 30 cm s^{-1}. The results from these tests are shown in figure 3.

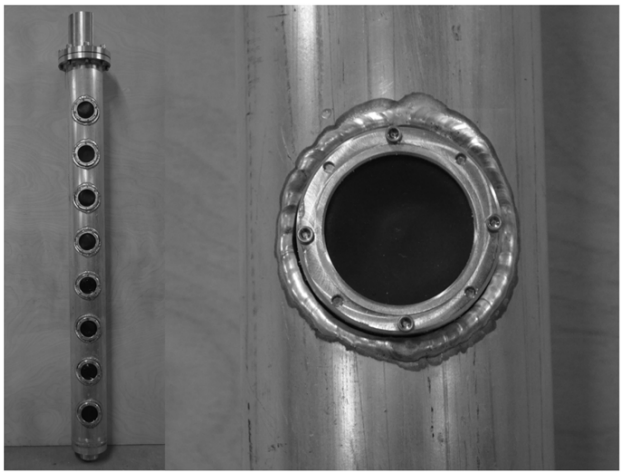

Figure 2. Field prototype.

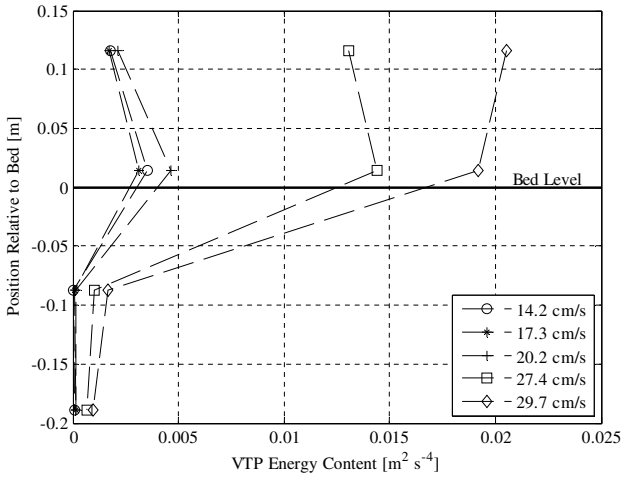

Figure 3. Performance of field prototype in CHL flume.

The results indicate that the VTP located in the channel flow and closest to the bed surface responds with an energy content that is at least one order of magnitude greater than the VTPs in the sediment. As was shown in Fisher *et al* [5], when the difference between the energy content of a VTP in the sediment and one located in the flow is at least one order of magnitude, the VTP method can determine the bed location. Additionally, the results in figure 3 indicate that for the velocity in the range of 14.2 to 20.2 cm s^{-1}, the energy content of the VTP near the bed varied from 0.0031 to 0.0046 m^2 s^{-4}. The difference between the VTP located in the flow and the sediment for these three cases ranged from a factor of 20 to 31. Thus, even for the low velocity cases, the field prototype still indicates the water/sediment interface and therefore can monitor any scour hole development. In the field, the VTP is partially buried in the riverbed and is secured to the bridge pier or abutment such that under normal conditions the flow is not skewed to the sensors. However, at low or high flows the flow may have skew with respect to VTP. Tests were conducted and the VTP was found to perform adequately up to 90 degrees skewed flow [6].

3. Modeling approach

The nature of the flows studied in fluid dynamics can be divided into two groups, laminar and turbulent. All natural channels flow under turbulent conditions. Fluctuations are present in all of the velocity components and pressure of a flow, which can be described through Reynolds' decomposition into the mean component, U, V and W in the three cardinal directions x, y and z (x is along the flow direction, y is normal to the bed and z is across the channel width), respectively, and the fluctuation components, u', v' and w' as shown in figure 4. Thus, when describing the instantaneous flow velocities, $\tilde{U}$, $\tilde{V}$ and $\tilde{W}$ at any point, it is necessary to include both components.

A similar expression can be developed for the pressure in the flow, $\tilde{P}$, which can be decomposed into its mean pressure, P, and the fluctuating component, p'. Based upon these definitions, it is necessary then that the time averaged values of $\tilde{U}$, $\tilde{V}$ and $\tilde{W}$ yield U, V and W, i.e. the long term time averaged values of u', v' and w' are zero. To get a measure of turbulence intensity, it is therefore necessary to use the

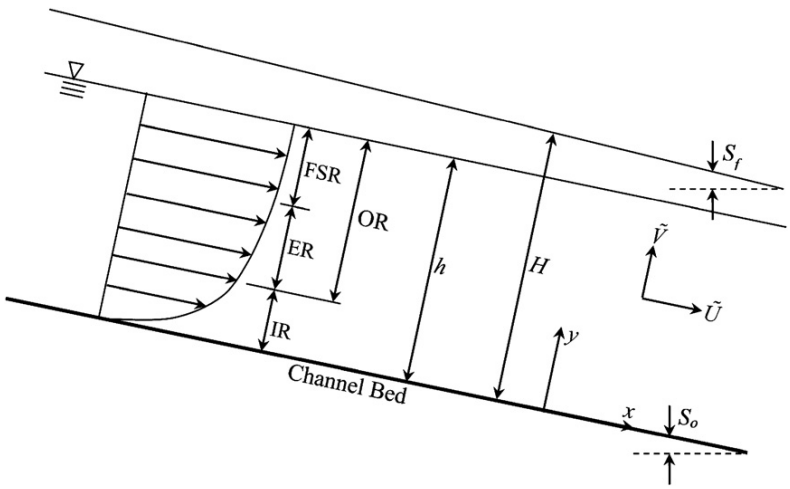

Figure 4. Channel parameters relevant to the Navier–Stokes equations.

root mean square (RMS) values of the fluctuating part of the velocities.

Turbulent flows are also characterized by eddy motions. Eddies are instabilities in the flow that are spatially and temporally correlated and are responsible for the velocity and pressure fluctuations. These eddies vary in size, with smaller eddies contained within larger eddies, up to the largest eddy in the flow. These eddies vary in scale from the molecular level where the smallest eddies are dissipated due to viscous forces as heat, to the large eddies which depend upon the size of the main channel [8]. The distribution of eddy sizes in the flow leads to the energy cascade from the larger eddies responsible for the production of turbulence to the small scale, low energy eddies responsible for the viscous dissipation of turbulence. The turbulent flow features discussed above will be utilized in developing a model to predict the response of a VTP under turbulent flow conditions.

3.1. Model for prediction of RMS values of fluctuating turbulent velocity

Wall bounded turbulent flows can be divided into two regions (figure 4), the inner region (IR) close to the wall, and the outer region (OR) near the free surface [9]. For all wall bounded flows, the IR is further decomposed into the viscous sub-layer (VSL), where viscous forces dominate, a buffer layer and the log-law layer (LLL). Adjacent to the LLL is the OR, which for open channel flows is affected by the presence of the free surface. The OR is broken down into the free surface region (FSR) and the equilibrium region (ER), which lies between the inner layer and the FSR. For smooth beds, the thickness of the VSL is defined as $\delta_V = 5\upsilon/U_*$, where υ is the kinematic viscosity of the fluid and U_* is the friction velocity. The VSL is typically small compared to the LLL [10]. Throughout the IR ($y/h < 0.2$), turbulence is generated by low speed streaks, which are ejected from the near wall region and subsequently burst [11, 12]. For rough boundary layers, as k_S (equivalent sand roughness) increases, the large eddies are interrupted by the roughness elements, leading to an increasingly isotropic turbulence [9]. Immediately outside the IR lies the ER ($0.2 < y/h < 0.6$), where neither the free surface nor wall effects dominate [9]. In this region, the rates of turbulent production and dissipation are approximately equal. The remaining OR ($0.6 < y/h < 1.0$) corresponds to the FSR, where the viscous dissipation exceeds any production of turbulence and is roughly equivalent to the rate at which turbulence is transported from the IR [12].

In the VSL, Prandtl's mixing length model leads to equation (1) [10, 13], where $U^+ = U/U_*$ and $y^+ = y\upsilon/U_*$. In the LLL, the mean flow can be described by equation (2). Based upon experimental evaluation, κ and A for open channel flows have been found to be 0.41 and 5.29 for smooth beds, respectively [13]. Equations (1) and (2) are valid for $y/h < 0.2$, additional models are required outside this region:

$$U^+ = y^+ \tag{1}$$

$$U^+ = \frac{1}{\kappa}\ln y^+ + A. \tag{2}$$

Coles [14] proposed that the deviation from the log-law in boundary layers outside of $y/h > 0.2$ could be accounted for with a wake function, Ψ. The resulting modification to equation (2) is shown in equation (3). The wake function parameter Π is equal to 0.55 for zero-pressure gradient boundary layers [10]:

$$\left.\begin{aligned} U^+ &= \frac{1}{\kappa}y^+ + A + \Psi \\ \Psi &= \frac{2\Pi}{\kappa}\sin^2\left(\frac{\pi}{2}\frac{y}{h}\right) \end{aligned}\right\}. \tag{3}$$

Thus, from equations (1), (2) and (3), it is possible to describe U^+ throughout the depth of open channel flows. Also, as $U_* = \sqrt{ghS_O}$ for uniform flow, it is also possible to describe U throughout the flow depth. Aside from the mean flow distribution in the channel, it is also necessary to describe the nature of the turbulent velocity fluctuations throughout the flow. Nezu [15] showed that the turbulence intensity terms (RMS values), outside the VSL are independent of the Reynolds number, Re, and Froude number, Fr, and can be described by equations (4), (5) and (6), with the empirically determined constants $D_U = 2.3$, $D_V = 1.27$, $D_W = 1.63$ and $C_K = 1$ [10]:

$$\frac{\sqrt{\overline{u'^2}}}{U_*} = D_U \exp\left(-C_K\frac{y}{h}\right) \tag{4}$$

$$\frac{\sqrt{\overline{v'^2}}}{U_*} = D_V \exp\left(-C_K\frac{y}{h}\right) \tag{5}$$

$$\frac{\sqrt{\overline{w'^2}}}{U_*} = D_W \exp\left(-C_K\frac{y}{h}\right). \tag{6}$$

Equation (7) is valid for the RMS value of u' in the VSL, which can be incorporated in equation (4) to describe the velocity fluctuations throughout the depth of the flow, as shown in equation (8) [10], where $Re_* = hU_*/\upsilon$, B has a value of 10 and $\Gamma = 1 - \exp(-y^+/B)$:

$$\frac{\sqrt{\overline{u'^2}}}{U_*} = 0.3y^+ \tag{7}$$

$$\frac{\sqrt{\overline{u'^2}}}{U_*} = D_U \exp\left(-\frac{y^+}{Re_*}\right)\Gamma + 0.3y^+(1-\Gamma). \tag{8}$$

3.2. Spectral model for turbulence

Velocity fluctuations lead to the driving force behind the operation of the VTP method, therefore it is necessary to determine the spectral content of these velocity fluctuations. Experiments have shown that the power spectral density of u', Φ_{uu}, are self-similar when appropriately normalized, even under different flow conditions. An appropriate model is developed to describe Φ_{uu}, which can be leveraged in modeling the response of a structure to turbulent flow.

The power spectral density can be related to the spatial correlation function, $R_x(r)$, as shown in equation (9), for two velocity measurements $u'(x)$ and $u'(x+r)$ separated by a distance r. Note that $R_x(r)$ can be measured experimentally. This correlation function has been shown to be an even function

[16], thus the power spectral density can be determined from the Fourier cosine transformation, as shown in equation (10):

$$R_x(r) = \frac{u'(x)u'(x+r)}{\overline{u'^2}} \tag{9}$$

$$\Phi_{uu} = \frac{2}{\pi}\int_0^\infty R_x(r)\cos(kr)\,\mathrm{d}r. \tag{10}$$

The power spectral density Φ_{uu} is independent of flow conditions and turbulent flow structure when normalized by the mean eddy macroscale, L_x. Several models for Φ_{uu} have been proposed to predict power spectral density for the production, inertial and viscous subranges of turbulent flows. The two models considered in this analysis are the von Karman and Heisenberg models. These models are typically described in wave number space, k. However, under Taylor's Hypothesis of frozen turbulence, it is possible to convert the parametric equations to frequency space, f, where $k = 2\pi f/\bar{U}$, where $\bar{U}$ is the depth-averaged mean flow velocity [12].

The von Karman spectra, shown in equation (11) [17] is a function of L_x and the characteristic wavenumber/frequency, k_o:

$$\Phi_{uu} = \frac{2}{\pi}L_x\overline{u'^2}\left(1+\left(\frac{k}{k_o}\right)^2\right)^{-5/6}. \tag{11}$$

The mean eddy macroscale can be determined from the measured correlation function, and corresponds to $L_x = \pi/2\Phi_{uu}(0)$ [12]. The distribution of L_x has been determined experimentally and can be described by the relationship shown in equation (12). The coefficient B_1 varies from 1.1 for Re_* of 600 to 1.0 for Re_* of 1600, where $Re_* = U_*h/\upsilon$ [9]:

$$\left.\begin{aligned}\frac{L_x}{h} &= B_1\left(\frac{y}{h}\right)^{1/2} \quad \text{for} \quad \frac{y}{h} < 0.6\\ \frac{L_x}{h} &= 0.77B_1 \quad \text{for} \quad \frac{y}{h} > 0.6\end{aligned}\right\}. \tag{12}$$

The characteristic wave number can be determined from mean eddy macroscale as shown in equation (13), where the parameter C is the Kolmogoroff constant with a value of 0.5 and K is given by equation (14) [9]:

$$k_o = \left(K\left(\frac{2}{\pi C}\right)^{-1.5}\right)^{-0.4}L_x^{-1} \tag{13}$$

$$K = 0.691 + 3.98\,(Re_L)^{-0.5}. \tag{14}$$

The Reynolds number, Re_L, in equation (14) is based upon the RMS value of u' for the velocity scale and L_x for the length scale. The von Karman model corresponds to the productive and inertial subranges of the turbulent energy spectral space, $0 \leqslant k \leqslant \lambda^{-1}$, where λ is the Taylor microscale of turbulence. Roughly, the von Karman model covers the open channel flow from the VSL to the ER. In the VSL, turbulence is produced and transported into the ER while in the ER the rate of production equals the rate of dissipation [12].

Another model is required to overlap the von Karman model from the inertial subrange to the viscous subrange, where the production is zero and the viscous dissipation equals the rate of transport. This is achieved with the Heisenberg model, shown in equation (15). The new terms introduced in equation (15) include the dissipation rate for turbulent energy, ε, the constant γ' and the Kolmogorov microscale of turbulence, η:

$$\overline{u'^2}\Phi_{uu}(k) = C\varepsilon^{2/3}k^{-5/3}(1+\gamma'(k\eta)^4)^{-4/3}. \tag{15}$$

The dissipation rate can be determined from equation (16). The u' terms are typically not measured to the resolution required to construct an accurate representation of equation (16). Therefore, it is common to exploit the isotropic turbulent assumption, leading to the right-hand side of equation (16) [9]. This assumption is an appropriate simplification, since turbulent fluctuations in all three directions are of the same order for open channels:

$$\varepsilon = 15\upsilon\left(\frac{\partial u'}{\partial x}\right)^2 = \frac{15\upsilon\overline{u'^2}}{\lambda^2}. \tag{16}$$

The Taylor and Kolmogorov microscales λ and η are defined as shown in equations (17) and (18), respectively. These microscales are practically solved via the fits employed in equations (19) and (20). Lastly, the constant γ' is taken as 100, as it gives the optimal fit with measured and published results from Kironoto and Graf [18] and Nakagawa and Nezu [9]:

$$\lambda = \sqrt{\frac{15\upsilon\overline{u'^2}}{\varepsilon}} \tag{17}$$

$$\eta = \left(\frac{\upsilon^3}{\varepsilon}\right)^{1/2} \tag{18}$$

$$\frac{L_x}{\lambda} = \left(\frac{K}{15}\right)^{1/2}Re_L^{1/2} \tag{19}$$

$$\frac{L_x}{\eta} = K^{1/4}Re_L^{3/4}. \tag{20}$$

The aforementioned model describes the RMS values of the turbulent flow quantities with depth, along with the spectral representation of the turbulent quantities. The next step is to calculate dynamic pressure due to these velocity fluctuations.

3.3. Dynamic pressure

In equation (4), the RMS value of u' is defined, which can be coupled with equations (11) and (15) to arrive at the spectral representation of the turbulent fluctuations in the open channel flow. These turbulent fluctuations lead to a time varying dynamic pressure, which excites the VTP. This spectrum is a function of the position across the channel depth. Given the variation of $\sqrt{\overline{u'^2}}$, the dynamic turbulent pressure impinging on the VTP disk can be determined by integrating the pressure distribution across the disk diameter, figure 5.

At a point in the flow, the dynamic turbulent pressure spectrum is computed as shown in equation (21). By integrating equation (21) across the VTP, the average pressure quantity, $\bar{\Phi}_{PP}$, can be computed as shown in equation (22), where r extends from the center of the VTP to the radius of the disk, R (see figure 5). It is not convenient to integrate $\Phi_{PP}(r)$, however it is possible to replace this term with a function of

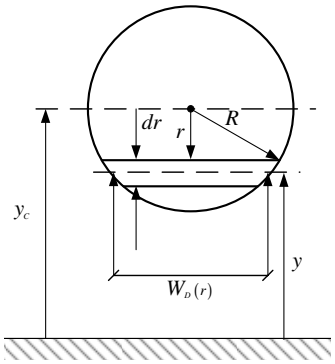

Figure 5. Area integration of dynamic turbulent pressure distribution across VTP disk.

y, as $y_C = y - r$. Additionally, the integrand in equation (22) can be replaced with the product of the differential radius dr and the element width, $W_D(r) = 2\sqrt{R^2 - r^2}$. The resulting expression is shown in equation (23):

$$\Phi_{PP} = \left(\frac{1}{2}\rho\overline{u'^2}\right)^2 \Phi_{uu} \tag{21}$$

$$\bar{\Phi}_{PP} = \frac{1}{A_{\mathrm{VTP}}}\int_{-R}^{R} \Phi_{PP}(r)\,\mathrm{d}A \tag{22}$$

$$\bar{\Phi}_{PP} = \frac{1}{A_{\mathrm{VTP}}}\int_{-R}^{R} \Phi_{PP}(r) W_D\,\mathrm{d}r. \tag{23}$$

3.4. Structural response

Having established the variation of the dynamic turbulent pressure across the channel depth, it is necessary to relate the dynamic pressure to the response of the VTP. Following the method outlined in Blevins [19], it can be shown that the response of a plate, for each mode, is described by equation (24), where ω_i is the undamped natural frequency of mode i in radians/second, ζ_i is the modal damping factor, J_i is the joint acceptance, $p_i(t)$ is the turbulent dynamic pressure averaged over a VTP as given by equation (23) and x_i is the displacement for mode i:

$$\frac{1}{\omega_i^2}\ddot{x}_i + \frac{2\zeta_i}{\omega_i}\dot{x}_i + x_i = J_i p_i(t)\,. \tag{24}$$

In the case where the joint acceptance is unity, the mode shape and the pressure distribution are spatially correlated for a given mode [19], and J is equal to 1. This results in the governing equation for a single degree of freedom oscillator. The steady state frequency response function of an oscillator, $|H(\omega)_i|^2$, to a random, stationary, ergodic and Gaussian pressure spectrum can be computed from equation (24) as shown in equation (25) [19]. As turbulence in open channels can be categorized as random, stationary, Gaussian and ergodic [19, 9, 20], the dynamic turbulent pressure determined by these velocity fluctuations can be categorized in the same manner:

$$|H(\omega)_i|^2 = \frac{1}{(1-(\omega/\omega_i)^2)^2 + (2\zeta_i\omega/\omega_i)^2}. \tag{25}$$

The response function shown in equation (25) represents the transfer function from the input force to the displacement response of the structure. The power spectral density of the displacement of the VTP can be computed from the product of equations (23) and (25). As the joint acceptance is not always unity, Blevins [21] suggests a correction method that requires the inclusion of the joint acceptance. Also, as the input force is derived from the dynamic pressure, the characteristic modal pressure, $\tilde{P}_{iC}$, is included to arrive at a displacement response spectrum. The characteristic modal pressure at the center of the VTP is shown in equation (26) [21]. The parameters in equation (26) are the density of the VTP disk, ρ_D, the disk thickness t and the displacement of the VTP center x_{iC}:

$$\tilde{P}_{iC} = \rho_D t\,(\omega_i)^2\,|x_{iC}|. \tag{26}$$

The above equation is then used to compute the displacement for mode i in physical units, Φ_{xxi}, as shown in equation (27). Further, due to the central limit theorem for random, independent processes, the mean squared sum of these processes is equal to the sum of the mean square of the individual processes. Thus, given that the turbulence in open channels is stationary and random, the overall displacement response spectrum of the VTP can be computed from the sum of the individual responses of each mode i, shown in equation (28):

$$\begin{aligned}\Phi_{xxi} &= \frac{\bar{\Phi}_{PP}}{(1-(\omega/\omega_i)^2)^2 + (2\zeta_i\omega/\omega_i)^2}\frac{J_i^2 x_{iC}^2}{P_{iC}^2} \\ &= \frac{\bar{\Phi}_{PP}}{(1-(\omega/\omega_i)^2)^2 + (2\zeta_i\omega/\omega_i)^2}\frac{J_i^2}{(\rho_D t(\omega_i)^2)^2}\end{aligned} \tag{27}$$

$$\Phi_{xx} = \sum_i \Phi_{xxi}. \tag{28}$$

Lastly, for random processes, the mean squared displacement response $\overline{x^2}$ can be related to the power spectral density, as shown in equation (29) [19]. Velocity and acceleration response spectra and mean squared response values can be derived from equations (28) and (29):

$$\overline{x^2} = \int_{f_1}^{f_2} \Phi_{XX}\,\mathrm{d}f. \tag{29}$$

To solve equation (27) it is necessary to include the natural frequencies and the modal damping factors. The natural frequency for a circular disk fixed at all boundaries (an appropriate approximation of the VTP device), can be calculated from equation (30), where E_D is the modulus of elasticity for the disk, ρ_D is the density of the disk, υ_D is Poisson's ratio for the disk and λ^2 varies from 10.22 to 21.26 for the first two modes [22]. An additional mode, which accounts for the mass of the accelerometer located at the center of the VTP is also required. The natural frequency for this mode can be calculated from equation (30), where λ^2 equals 5.34, as discussed in Roberson [23]:

$$\omega_i = \frac{\lambda^2}{r^2}\left(\frac{E_D t}{12\rho_D t\left(1-\upsilon_D^2\right)}\right)^{1/2}. \tag{30}$$

Another component of equation (27) is the modal damping factor. Due to the presence of the fluid around the VTP disk, this damping will consist of the damping from the disk material

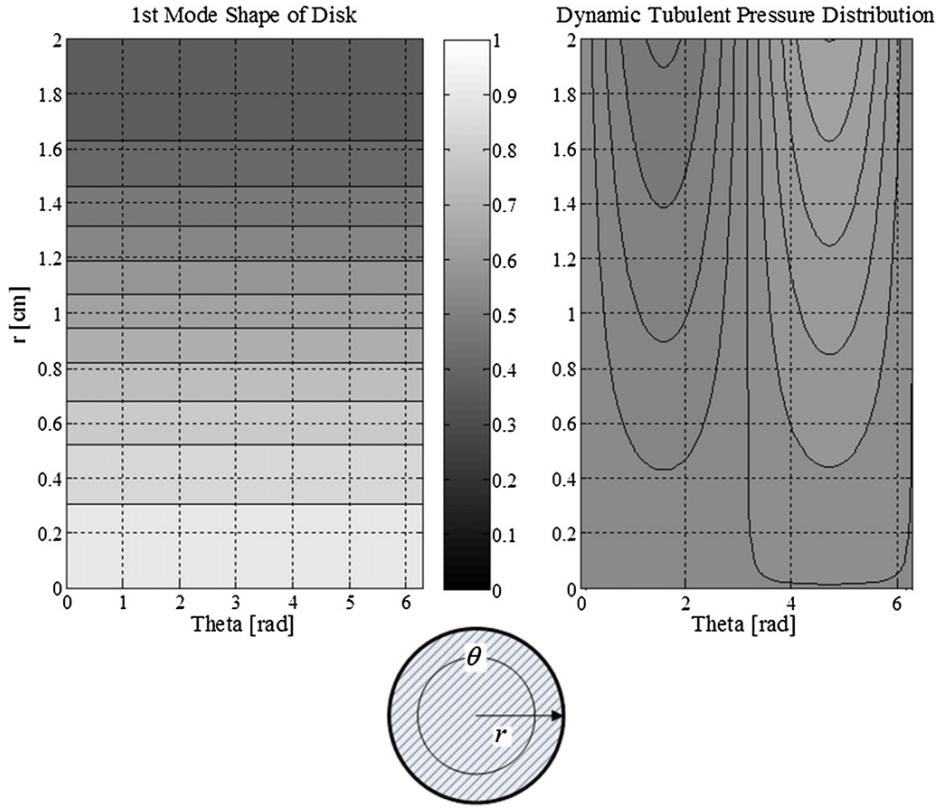

Figure 6. Components of the joint acceptance for the first plate mode.

itself, ζ_s, taken as 0.05 [24], and the fluid damping ζ_f. For moving channel fluid, the fluid damping can be estimated from equation (31) with an appropriate substitution of the drag coefficient, C_D, taken as 1.28 for a plate in cross flow, and $\tilde{m}$ as the mass per unit length of the disk [19]:

$$\zeta_f = 2\frac{U}{\omega_i D}\frac{\rho R^2}{\tilde{m}t}C_D. \tag{31}$$

Finally, it is necessary to consider the assumption regarding the joint acceptance. The joint acceptance can be computed from the mode shape, $\tilde{x}_i\,(r,\theta)$, and the pressure distribution, $\tilde{P}_i\,(r,\theta)$, (normalized by $m\,(\omega_i)^2$ for each mode) as shown in equation (32) [22]. The parameters in equation (32) are the mass per unit area m and angle θ, which varies from 0 to 2π:

$$J_i = \frac{\int_A \tilde{P}_i(r,\theta)\tilde{x}_i(r,)\,\mathrm{d}r\,\mathrm{d}\theta}{\omega_i^2\int_A m\tilde{x}_i^2(r,\theta)\,\mathrm{d}r\,\mathrm{d}\theta}. \tag{32}$$

For the first mode of the VTP disk, the mode shape and dynamic turbulent pressure distribution are shown in figure 6. For the first three modes the joint acceptance values are 1.11, 1.06 and 1.83, respectively. The natural frequency of the subsequent modes, as will be shown in section 4, are greater than 500 Hz, typically outside the range of the VTP response spectra and subsequently have a negligible impact on the mean squared response value. The joint acceptance values listed above are incorporated into the analytical model, equation (27).

4. Model verification, calibration and validation

A numerical model is prone to errors that originate from the mathematics and the physics of the problem. The errors and uncertainties introduced while solving the mathematical equations include round-off, discretization and truncation errors. These errors are accounted for under the broad topic of model verification. The second source of error in a model arise from uncertainties introduced from an imperfect model definition of underlying physical principles as well as the imprecise values for the associated parameters of the chosen model [25]. Models and their associated parameters can be conditioned based on the experimental data to reduce the uncertainties and infer biases in model predictions. It is important to note that validation of a model requires a data set independent from those that are used in the calibration step [26].

The following sections assess the predictive capabilities of the developed semi-empirical model. The verification activities involve investigation of the impact of the dynamic pressure integration across the VTP. This is then followed by a calibration of the model performance to an experimental data set in order to account for the variability inherent in the model input parameters. Finally, the model is validated by comparing the predictions against an independent data set.

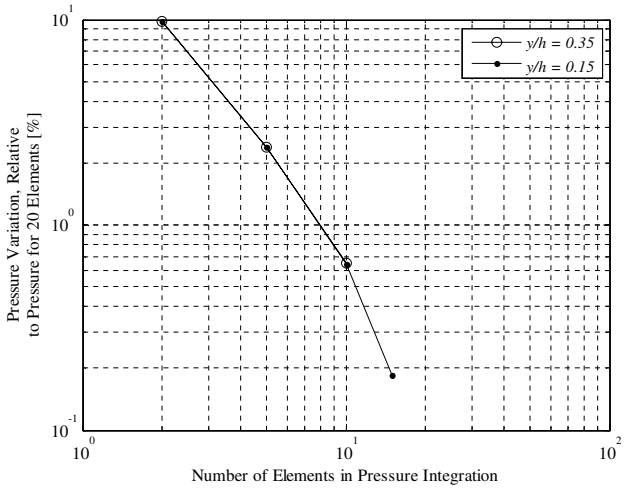

Figure 7. Variation in VTP turbulent pressure, as a function of number of elements.

4.1. Model verification

It has been well documented [13] that the variation of u' across the channel depth is nonlinear, with the peak occurring near the bed. Given that the VTPs are designed to typically operate at $y/h < 0.3$, it is necessary to consider the variation in the turbulent velocity fluctuations across the depth of the VTP surface (generally having a diameter from 4 to 6 cm). In equation (23) this is accounted for by integrating the pressure distribution, which is dependent on u', across the disk surface. To investigate the effect of the numerical integration step width, dr, used in equation (23), the pressure is integrated with decreasing step width, as shown in figure 7. The results reveal that after 10 integration step widths, the result for both y/h of 0.15 and 0.35 are within 1% of the 20 step width result. From this result, it can be concluded that 15 step widths are sufficient to capture the pressure variation across the VTP.

4.2. Model calibration

4.2.1. Structural dynamic model. The parameter values used in the development of the model, reviewed in section 3, are best estimates obtained from literature review. Therefore, it is necessary to condition the parameter values against the actual measured response of the structure. The parameters considered in this calibration include the disk material properties, E_D, ζ_D and ρ_D, as well as the turbulent flow characteristics, U_*, ζ_F and $\sqrt{\overline{u'^2}}$. The calibration of the disk parameters is accomplished by conducting an experimental modal analysis on the VTP disk and calibrating the natural frequencies to the measured natural frequencies. The calibration of the turbulent flow quantities is accomplished via experiments conducted in the CHL flume.

To calibrate the natural frequency predictions for the various modes in the VTP, model predictions are compared with the measured natural frequencies for a 3.2 mm thick, 2.54 cm radius, neoprene rubber VTP. The measured values are obtained by rigidly fixing the VTP and attaching a shaker to the disk surface. The force transmitted to the plate is measured with a Bruel and Kjaer 8200+2646 force transducer, with a sensitivity of −4 mV N^{-1}. The acceleration response of the VTP is recorded with a Kistler 8732A500 accelerometer, with a sensitivity of 9.64 mV g^{-1}. The neoprene test is conducted with a span of 800 Hz and 6400 lines, leading to a frequency resolution of 125 mHz. The shaker ranges bi-directionally for 1 to 1000 Hz at a rate of 125 Hz s^{-1}.

Table 1. Model and measured natural frequencies for modes in neoprene.

	Neoprene 30A			Calibrated results	
Mode shape	Model	Meas.	% Error	Model	% Error
1[a]	80.17	70.3	14		
2	248	292	−15	260	−11
3[b]	NA	366	NA	NA	NA
4	515	534	−3.6	540	1.1
5	845	773	9.3	886	15
6	963	903	6.6		

[a] Affected by stringer mass and stiffness.
[b] Stringer/plate coupled mode.

The comparisons between the calculated and measured natural frequencies are shown in table 1 for the first six modes. For the higher modes, the prediction results are within 10% of the measured frequencies. The first mode is calculated including the presence of the accelerometer as a point mass. Model calibration can be completed to minimize the disagreements between the measured and calculated natural frequencies considering all six modes. However, the disagreement observed for the first mode is believed to be due to the stringer connecting the shaker to the VTP sensor. Also, the third observed mode is believed to be a spurious mode resulting from the interaction between the stringer and the VTP, which is not included in the model. Therefore, the first and the third modes are excluded from the calibration activities.

The natural frequencies presented in table 1 are dependent upon the model parameters E_D, ρ_D, t and R. The geometric parameters t and R are design parameters, which can be controlled during the manufacturing of the prototype, and thus are known with high certainty. Furthermore, the density parameter can be measured with relative ease and high accuracy. Therefore, the only remaining parameter that is poorly-known is the Young's Modulus of the plate, which nominally is 8.3 MPa. An optimal fit is achieved considering modes 2, 4 and 5 with a 10% increase in the modulus of the disk while all other remain at their nominal values. The results of this analysis are also shown in table 1. As indicated, the fits of modes 2 and 4 improve with the calibration in the model parameters. This represents an optimal fit since the contribution of each mode to the overall response is not equal. Mode 2 contributes 100 times more to the overall measured acceleration response than mode five. Thus a 4% reduction in the percent error for mode 2 is significant.

4.2.2. Turbulence model. To calibrate the turbulence characteristics developed in the semi-empirical model, channel velocity is measured in the CHL flume with a Sontek acoustic Doppler velocimeter (ADV), A701F, at 50 Hz. The sample

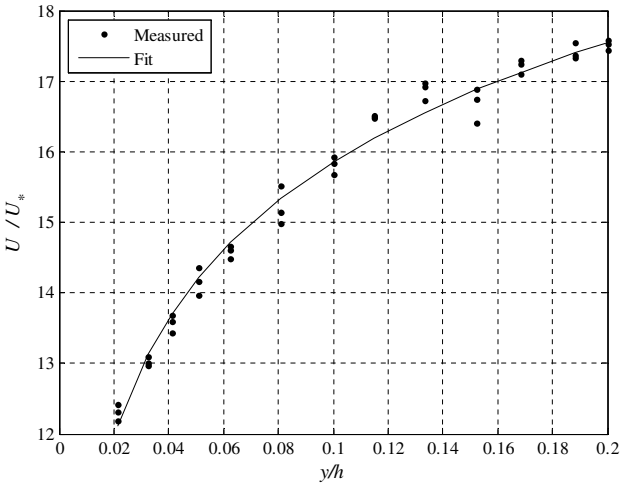

Figure 8. Distribution of U/U_* as a function of depth in the channel, for run 1.

Table 2. Flow parameters for CHL flume tests.

Run	h (cm)	U (cm s^{-1})	U_* (cm s^{-1})	Re_*
1	29.3	35.7	2.2	6360
2	26.4	31.1	1.4	3710
3	32.7	27.4	1.6	4560

time of 5 min is found to adequately capture all eddy scales. The flume bed consists of quartz sand with a median grain size of 1.5 mm. The velocity measurements are made throughout the depth, from y/h of 0.10 to 0.60. Pertinent flow parameters for each of the three runs are shown in table 2.

It is also necessary to determine the value for U_*, an input for the turbulent channel flow model. This can be accomplished from the measured results in two ways. Equation (2) can be fit, using the least squares method, to the measured values of U within the LLL. The coefficient of this fit is equal to the quotient of U_* and κ. Since the von Karman constant is known, this coefficient can be solved for the friction velocity. A second approach considers the contribution of the velocity gradient and the turbulent shear stress to the bed shear stress. The offset of a liner fit through the product $-\rho u'v'$ as a function of y is equal to the bed shear stress, τ_o, which can be related to the friction velocity, as in equation (33). These two methods yield similar results for runs 1–3. The friction velocity values shown in table 2 are based on the first method. The fit through these data points are shown in figures 8 and 9:

$$U_* = \sqrt{\frac{\tau_o}{\rho}}. \tag{33}$$

With U_* determined, it is then possible to compute the analytical model response for the turbulent fluctuations as a function of depth. The velocity fluctuations are computed using equation (4) and compared with the measured results, as shown in figure 10. The coefficient of determination between the measured values and the model is 0.73 for run 1, 0.87 for run 2 and 0.82 for run 3, indicating an acceptable representation of the measured data by the turbulence model.

In addition to the turbulent velocity fluctuations, the semi-empirical model must accurately represent the velocity spectra.

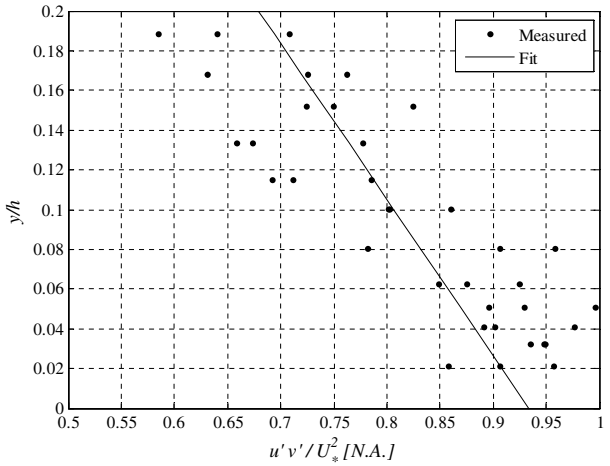

Figure 9. Distribution of $u'v'$, as a function of depth in the channel, for run 1.

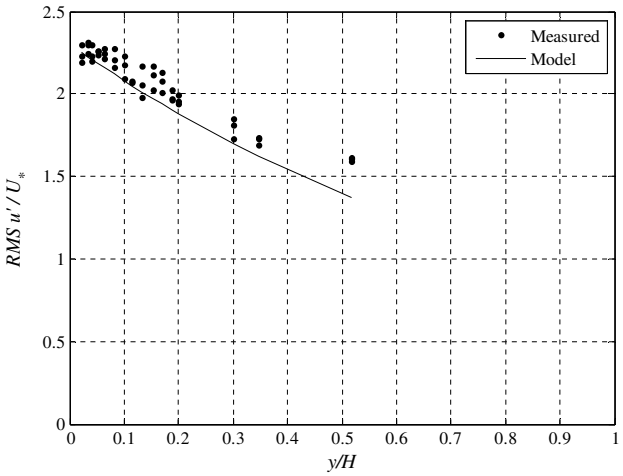

Figure 10. Measured and model root mean square of u' ratio with friction velocity, as a function of depth in the channel (run 1).

Several spectra are available in the published literature, two of which are shown in figures 11 and 12. Figure 11 shows the comparison of the model predictions against the data published by Kironoto and Graf [18]. As shown in the figure, the model fit falls within the published data set. The coefficient of determination is 0.89. Similarly, the comparison of the model results with the data published by Nakagawa and Nezu [9] are shown in figure 12, where the coefficient of determination is 0.97. The results shown in figure 12 indicate that the model captures the same trend as the measured data.

Turbulent spectra can also be constructed from the measured ADV data for runs 1–3. The power spectral density of the turbulent velocity fluctuations for run 1, for y/h of 0.1, 0.2 and 0.3 are shown in figures 13–15, respectively. The results indicate that the model captures the shape and magnitude of the measured turbulent spectra, with coefficient of determination of 0.87, 0.79 and 0.92, respectively. For the higher frequencies, the model results under predict the measured spectra. This deviation is expected due to the nature of the ADV measurements. It is possible to correct

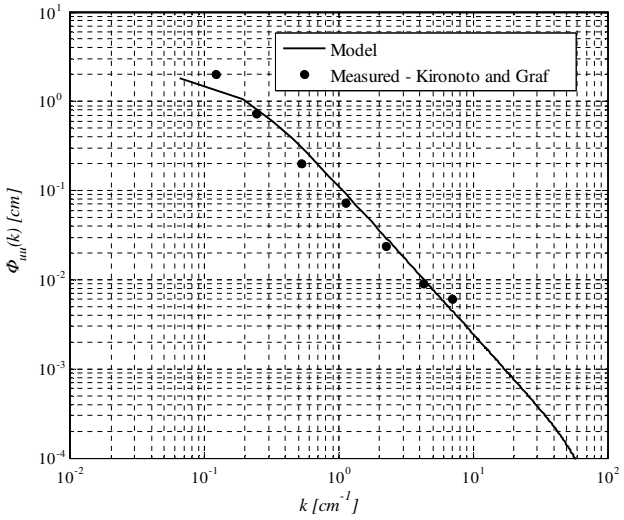

Figure 11. Comparison of model turbulent velocity fluctuation spectra with published results from Kironoto and Graf [18].

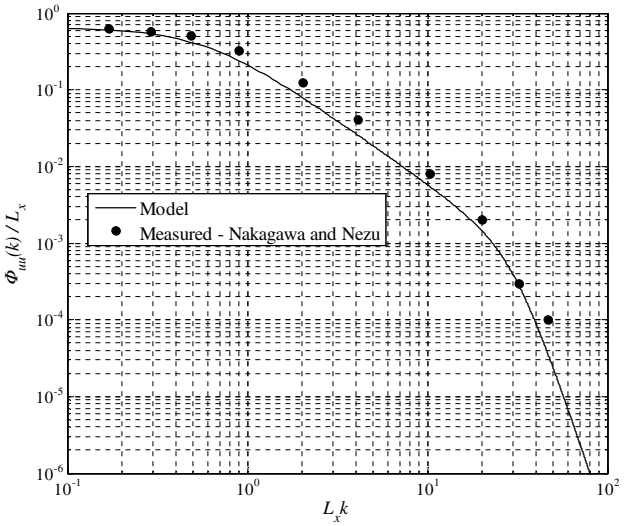

Figure 12. Comparison of model turbulent velocity fluctuation spectra with published results of Nakagawa and Nezu [9].

the measured data as discussed in Hurther and Lemmin [27]. However, this requires a sonar device with a fourth probe to correct for the noise in the measured signal. The Sontek ADV device used in this study is not equipped with this additional probe, so this correction is not possible.

Figures 11–15 reveal that the power spectral density of the u' velocity fluctuations as presented in the turbulence model are in agreement with both published spectra and those measured in the flume. In addition, the magnitudes of the velocity fluctuations, shown in figure 10, correspond to the measured values obtained with the ADV measurements. Thus, it can be concluded that the semi-empirical model component for the turbulent open channel flow does not require calibration in order to predict the magnitude and spectra of u'.

The objective of the overall semi-empirical model is to predict the mean squared acceleration response of the VTP.

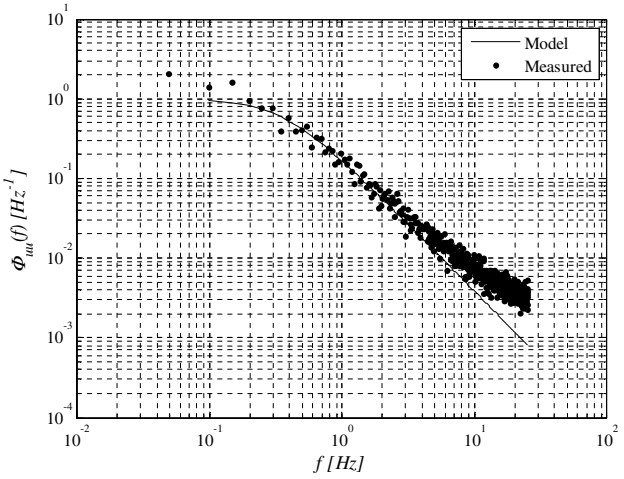

Figure 13. Power spectral density of u' at a y/h of 0.1, from run 1.

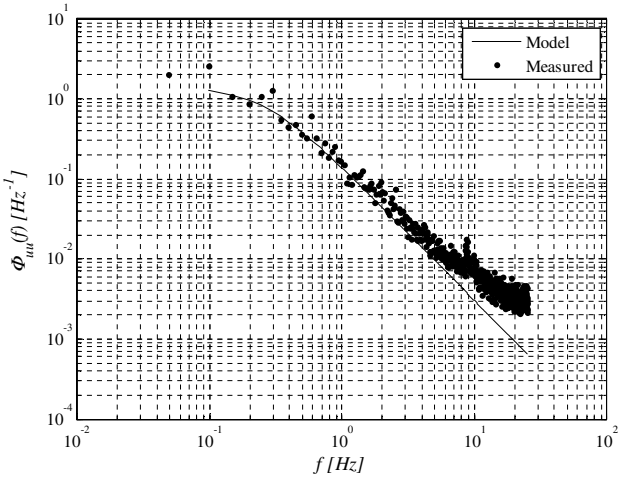

Figure 14. Power spectral density of u' at a y/h of 0.2, from run 1.

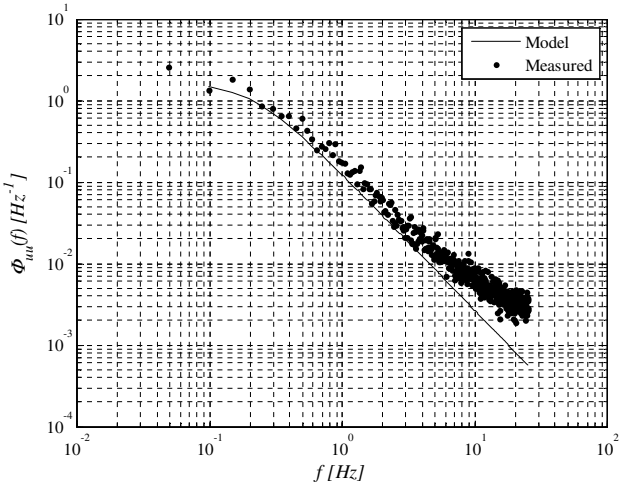

Figure 15. Power spectral density of u' at a y/h of 0.3, from run 1.

These results will also have to be calibrated in order to use the model for prediction and optimization of the VTP for field

deployment. Data sets corresponding to the conditions for run 1 are recorded experimentally, as discussed in Fisher *et al* [5], and are used to calibrate the model result. The measured VTP energy content response is recorded at y/h of 0.16 and 0.51. The mean energy content from this data set for the lower VTP is 0.0220 $m^2\ s^{-4}$ with a standard deviation of 0.0015 $m^2\ s^{-4}$. The model predictions for this VTP's mean energy content is 0.14 $m^2\ s^{-4}$. For the upper VTP, the mean energy content is 0.0150 $m^2\ s^{-4}$ with a standard deviation of 0.0011 $m^2\ s^{-4}$. The model predictions for this VTP's mean energy content is 0.0063 $m^2\ s^{-4}$. Based upon these results, it is necessary to calibrate the model. The objective of the calibration is to configure the results such that the model predictions are within ten times the standard deviation of the measured energy contents for the various positions within the channel. This will result in a calibrated model that can predict the VTP energy response within the appropriate order of magnitude but does not overly constrain the response. Since the model is being used to determine the geometry of the prototype, this will ensure that the predicted results are sufficiently accurate to capture the difference between VTPs located in the sediment and in the flow.

The remaining parameters under consideration for calibration include the combined structural and fluid damping, the friction velocity, the mean flow velocity and a factor introduced in equation (21) that accounts for variations in the proportionality of the turbulent velocity fluctuations to the dynamic pressure. These parameters are varied by up to 20%. The largest variation in the model response occurs for the friction velocity, resulting in a variation in the mean energy content of up to 80%. Given this variability in the model results, U_* is chosen for calibration. Based upon the measured variation in the model response as a function of position within the channel flow, the friction velocity is calibrated by a linear function of position, with a slope of 0.833 and an intercept of 0.668. The resulting model predictions are 0.0367 and 0.0150 $m^2\ s^{-4}$ for y/h for 0.16 and 0.51, respectively, a significant improvement in the model results.

The obtained model is conditioned based on the measured data during calibration, and thus it is necessary to validate the model by comparing the predictions against an independent data set.

4.3. Model validation

The data set used for validating the analytical model consists of the measurements taken during run 3, an independent data set not used for calibration. The measured VTP responses are recorded at positions in the channel of y/h for 0.35 and 0.66. The measured energy content response for each VTP is 0.013 and 0.0079 $m^2\ s^{-4}$ for the lower and upper VTPs, respectively. Using the calibrated model, the predictions are 0.0158 and 0.0075 $m^2\ s^{-4}$ for these two positions, which are within the desired model tolerance.

In addition to computing the mean squared energy content response for the VTPs, it is also possible to compare the measured acceleration power spectral density with the model predictions. For the two VTP positions, the measured and model acceleration power spectra are shown in figures 16 and 17, respectively. In addition to the synthesized modal response of the VTP, the first three modes of the VTP are also shown in order to highlight their contribution to the overall response. As shown in figures 16 and 17, the results indicate that the first mode is responsible for the majority of the low frequency response. The model response for the first mode also indicates that the model mode is underdamped relative to the measured response. This suggests that further refinements in the model are possible. However, given that the objective of the model development is to optimize a field deployable scour monitoring device, the current model precision is acceptable.

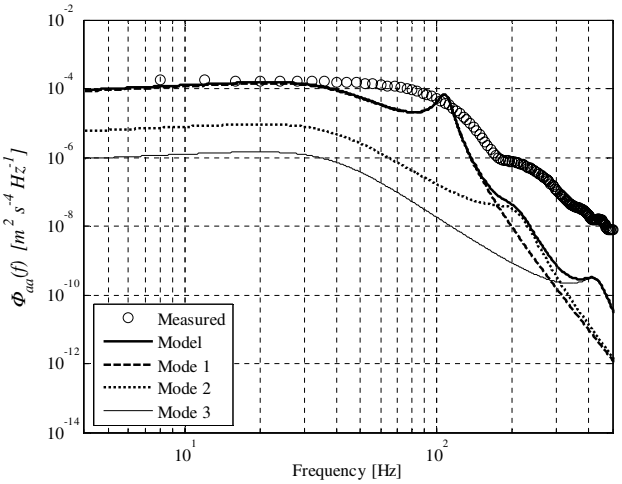

Figure 16. Measured and model acceleration response spectra for run 3 conditions, y/h of 0.35. VTP plate is 1.6 mm thick, 2 cm radius neoprene.

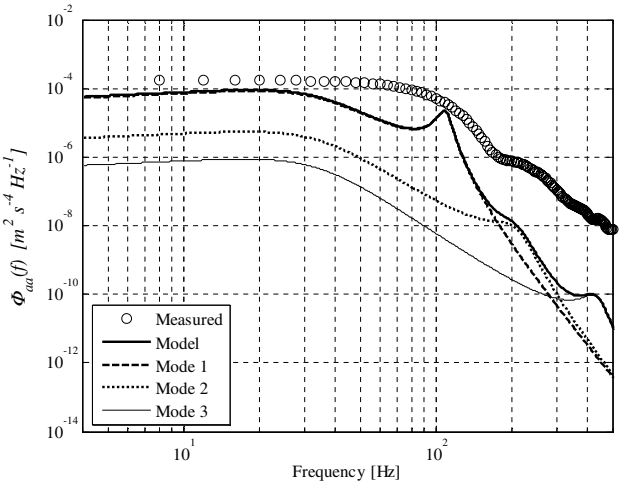

Figure 17. Measured and model acceleration response spectra for run 3 conditions, y/h of 0.66. VTP plate is 1.6 mm thick, 2 cm radius neoprene.

In addition to the validation activities discussed previously, it is also worthwhile considering how the model performs in off-design conditions. To investigate this, the field prototype is also tested against varying flow misalignment between the main flow and the VTP axis. The results from

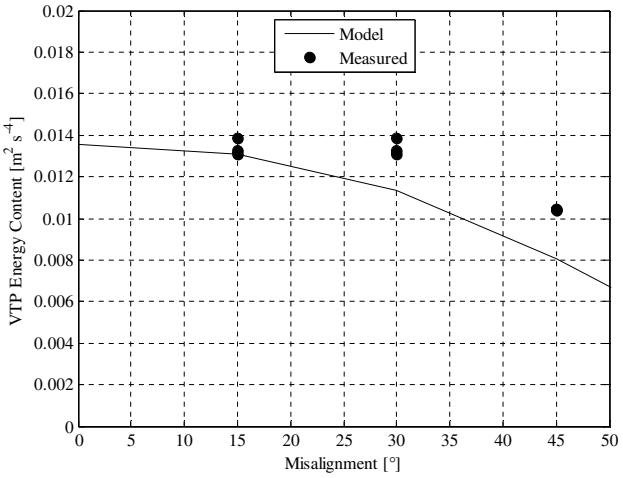

Figure 18. Measured and analytical model response as a function of flow misalignment.

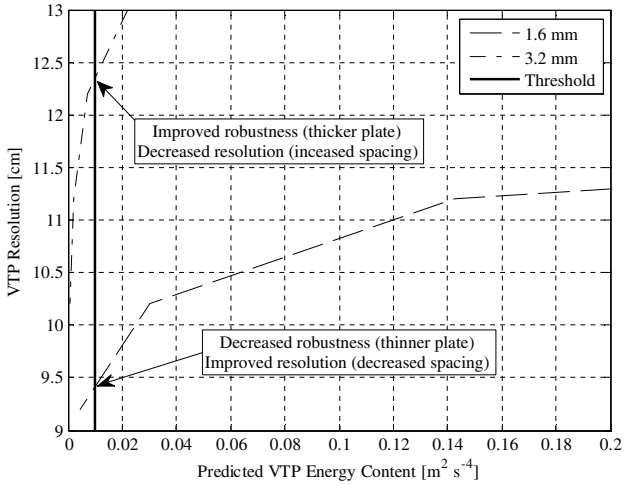

Figure 19. Optimization of VTP size and thickness for field deployment.

these tests are compared against the semi-empirical model, which is shown in figure 18.

The model and measured results reveal that as the misalignment increases, the response from the VTP decreases. The model response approaches the measured results for smaller angles of misalignment. As the misalignment increases, the model results begin to deviate from the measured results. This is expected, as the flow around the probe will begin to separate at the upstream edge of the VTP with increasing misalignment. This effect is not accounted for in the analytical model. Despite this, the model is able to capture the measured decay in energy content with increasing misalignment. This serves to further confirm that the semi-empirical model is capturing the governing physics that dictate the VTP energy content response.

5. VTP optimization for field deployment

The VTP-based method is shown to be an effective means for monitoring the formation of scour holes in natural channels (see figure 3). Additionally, the semi-empirical model provides a description of the interaction of the VTP structure and the turbulent open channel flow (see figures 16–18). Since the model is verified, calibrated and validated, it is also appropriate to use the model to consider changes to the VTP energy content as the device is modified. The following discussion considers the competing desire to improve the VTP's resolution, while also ensuring the final device is robust for deployment in a natural channel.

Fisher *et al* [5] has already shown that nonmetallic disks for the VTP are preferred over metallic disks, due to the lower stiffness, and higher acceleration response for a given turbulent dynamic pressure. Additionally, it has already been shown that circular VTPs are preferred over square geometries. Therefore, the optimization for field deployment considers only the radius (resolution) and thickness (robustness) of the disk as design parameters.

From the measured results of the VTP energy content presented in Fisher *et al* [5] and shown in figure 3, it was determined that the maximum response from the VTPs located in the sediment was 0.009 m^2 s^{-4}. In order to ensure the response of the VTP located in the flow is at least one order of magnitude greater than the VTPs in the sediment, a threshold energy content value is set to 0.01 m^2 s^{-4}. This ensures that the VTP device can be used for scour monitoring. Additional constraints imposed on the optimization process included that the resolution of the device is equal to that of a magnetic sliding collar, which can resolve the bed depth to 0.15 m [1]. Also, the material selected should be able to withstand the conditions that are likely to occur in the field. Given the performance of the neoprene in the experimental results conducted previously, the decision is made to select this material for the field deployment.

Based upon the conditions discussed previously, several predictions are made with the analytical model for VTP thicknesses of 1.6–3.2 mm and radii from 1.5 to 3.5 cm. A minimum spacing of 6.2 cm between adjacent VTPs is required for the additional hardware necessary to mount the sensors. It is possible to consider the VTP response versus the resolution of the VTPs, as shown in figure 19. The optimal VTP will respond above the required threshold and with a minimum spacing (leading to an improved resolution).

The results reveal that the VTP with optimal resolution (10.2 cm) corresponds to a VTP with a thickness of 1.6 mm and a radius of 2 cm. The most robust VTP (3.2 mm thickness) corresponds to a VTP with a radius of 3.5 cm and a resolution of 13 cm. From these results, it is determined that the 1.6 mm, 2.0 cm radius is preferred over the thicker and larger VTP due to the improved resolution achievable with the smaller device. The model also indicates that the energy content to be higher for the thinner VTPs for the same dimension. Therefore, it is anticipated that the minimum flow rate required for excitation of the smaller, thinner VTP will be lower than that of the larger, thicker VTP.

Additional uses for the semi-empirical model are possible, such as training an interpolation fit to the measured energy content for a particular installation in order to improve the ability to determine the riverbed location.

These considerations, however, remain avenues for further exploitation of the semi-empirical model with field data.

6. Summary and conclusions

Given the desire to monitor the progressive formation of scour holes around bridge piers and abutments, the VTP-based method is proposed as an alternative method that exploits the turbulence in natural open channels. Experimental results presented reveal the utility of a field deployable device constructed with eight VTPs. The performance of the device in off-flow conditions is also presented.

In addition, a semi-empirical model that can predict the energy content response of a flexible plate to turbulent open channel flow is developed. This model includes an empirical relationship between channel conditions and turbulent velocity fluctuations. The turbulent flow model is coupled to a dynamic structural response model which translates variations in the dynamic turbulent pressure impinging on the VTP into a prediction of the mean acceleration response.

A mesh refinement study is completed to determine the number of elements across the VTP surface required during integration of surface pressure. The study shows that result converge to within 1% of its final value for ten integration step-widths. Furthermore, the first three natural frequencies are calibrated with a 10% increase in the modulus for the neoprene disk. The turbulent model calibration is investigated and reveals that the measured and predicted values are within the expected measurement error and is not adjusted. The final calibration showed that the model is sensitive to the friction velocity, which is then calibrated against a measured data set.

The calibrated model is then validated against an independently measured data set and reveals that the predicted values are within the desired tolerance of 0.015 m^2 s^{-4}. The predicted responses from the calibrated model range from 3 to 22% of the measured energy content responses for the independent data set. This represents a significant improvement in the model over the uncalibrated model.

In addition to describing the physical operation of the VTP device, the semi-empirical model provides the added benefit of allowing for optimization of the device for the field. The VTP is optimized for both robustness to the channel environment and for improved riverbed detection resolution. The optimal device configuration for a robust VTP was determined to be 3.5 cm radius, 3.2 mm thick plate, which has a resolution of 13 cm. Conversely, the optimal VTP for resolution corresponds to a 1.6 mm thick, 2 cm radius plate, which has a resolution of 10.2 cm.

Further uses for the model are also proposed, such as considering the nature of the energy content profile across the channel depth. It is possible to conceive of a curve that can be fit to measured field profiles, using the semi-empirical model as a guide. This would allow for further refinement of the measured riverbed location.

Acknowledgment

The authors would like to thank the South Carolina Department of Transportation for supporting this work through grant number 1417.

References

[1] Lagasse P F, Richardson E V, Schall J D and Price G R 1997 Instrumentation for measuring scour at bridge piers and abutments *NCHRP Report* 396 TRB, National Research Council, Washington, DC

[2] Lagasse P F, Clopper P E, Pagán-Oriz J E, Zevenbergen L W, Arneson L A, Schall J D and Girard L G 2009 Bridge scour and stream instability countermeasures: experience, selection and design guidance *Hydraulic Engineering Circular No. 23* 3rd edn, Publication No. FHWA-NHI-09-111, US Department of Transportation, Federal Highway Administration

[3] Brice J C and Blodgett J C 1978 Countermeasures for hydraulic problems at bridges vol 1 & 2 FHWA/RD-78-162 & 163, Federal Highway Administration, US Department of Transportation, Washington, DC

[4] Rhodes J and Trent R 1993 Economics of floods, scour and bridge failures *Hydraulic Engineering '93: Proc. 1993 Conf. (San Francisco, CA, 25–30, July 1993, ASCE)* ed H W Shen, S T Su and F Wen pp 928–33

[5] Fisher M, Atamturktur S and Khan A A 2013 A novel vibration-based monitoring technique for bridge pier and abutment scour *Struct. Health Monit.* **12** 114–25

[6] Fisher M, Chowdhury M N, Khan A A and Atamturktur S 2013 An evaluation of scour measurement devices *J. Flow Meas. Instrum.* **33** 55–67

[7] Bruer M and Münch M 2008 Fluid–structure interaction using LES—a partitioned coupled predictor—corrector scheme *Proc. Appl. Math. Mech.* **8** 10515–6

[8] Panton R L 2005 *Incompressible Flow* 3rd edn (Hoboken, NJ: Wiley)

[9] Nezu I and Nakagawa H 1993 *Turbulence in Open-Channel Flows IAHR, AIRH Monograph* (Rotterdam, The Netherlands: AA Balkema)

[10] Nezu I 2005 Open-channel flow turbulence and its research prospect in the 21st century *J. Hydraul. Eng. ASCE* **131** 229–46

[11] Davidson P A 2004 *Turbulence, an Introduction for Scientists and Engineers* (New York: Oxford University Press)

[12] Nakagawa H, Nezu I and Ueda H 1975 Turbulence of open channel flow over smooth and rough beds *Proc. Japan Soc. Civ. Eng.* **241** 155–68

[13] Nezu I and Rodi W 1986 Open-channel flow measurements with a laser Doppler anemometer *J. Hydraul. Eng. ASCE* **112** 335–55

[14] Coles D 1956 The law of the wake in the turbulent boundary layer *J. Fluid Mech.* **1** 191–226

[15] Nezu I 1977 Turbulent structure in open-channel flows *PhD Thesis* Kyoto University, Kyoto, Japan

[16] Meecham W C 1958 Relationship between time symmetry and reflection symmetry of turbulent fluids *Phys. Fluids* **1** 408–10

[17] von Karman T 1948 Progress in the statistical theory of turbulence *Proc. Natl Acad. Sci.* **34** 530–9

[18] Kironoto B A and Graf W H 1994 Turbulence characteristics in rough uniform open-channel flow *Proc. ICE, Water Marit. Energy* **106** 333–44

[19] Blevins R D 1990 *Flow Induced Vibration* (New York: Van Nostrand-Reinhold)

[20] Galanti B and Tsinober A 2004 Is turbulence ergodic? *Phys. Lett.* A **330** 173–80

[21] Blevins R D 1977 An approximate method for sonic fatigue analysis of plates and shells *J. Sound Vibration* **129** 51–71
[22] Blevins R D 1979 *Formulas for Natural Frequency and Mode Shape* (New York: Van Nostrand-Reinhold)
[23] Roberson R E 1951 Vibration of a clamped circular plate carrying concentrated mass *West Coast Conf. of the Applied Mechanics Division, The American Society of Mechanical Engineers (Stanford, CA, 22–23 June 1951)* pp 349–52
[24] Berger E H, Royster L H, Royster J D, Driscoll D P and Layne M 2003 *The Noise Manual* 5th edn (Fairfax, VA: American Industrial Hygiene Association)
[25] Atamturktur S, Hemez F M and Laman J A 2012 Uncertainty quantification in model verification and validation as applied to large scale historic masonry monuments *Eng. Struct.* **43** 221–34
[26] Trucano T G, Pilch M and Oberkampf W L 2002 General concepts for experimental validation of ASCI code applications *Sandia National Labs, Report No.* SAND2002-0341
[27] Hurther D and Lemmin U 2001 A correction method for turbulence measurements with a 3D acoustic Doppler velocity profiler *J. Atmos. Ocean. Technol.* **18** 446–58